Progress In Electromagnetics Research B, Vol. 30, 177–199, 2011

MEASURED COMPLEX PERMITTIVITY OF WALLS WITH DIFFERENT HYDRATION LEVELS AND THE EFFECT ON POWER ESTIMATION OF TWRI TARGET RETURNS

C. Thajudeen, A. Hoorfar, and F. Ahmad

Center for Advanced Communications
Department of Electrical and Computer Engineering
Villanova University, Villanova, PA 19085, USA

T. Dogaru

US Army Research Lab, Adelphi, MD 20783, USA

Abstract—In this paper, measured results for complex permittivity of some commonly used building walls under different hydration (wetness) levels are presented and a simple hybrid measurement and electromagnetic modeling approach for the estimation of power returns from targets located behind walls in various through-the-wall radar imaging (TWRI) scenarios is discussed. The radar cross section (RCS) of some typical targets of interest, such as an AK47 assault rifle and human, are first investigated in free-space using numerical electromagnetic modeling. A modified radar range equation, which analytically accounts for the wall effects, including multiple reflections within a given homogeneous or layered wall, is then employed in conjunction with wideband measured parameters of various common wall types, to estimate the received power versus frequency from modeled targets of interest. The proposed technique, which can be helpful in TWRI dynamic-range system design consideration, is, in principle, applicable to both bistatic and monostatic operations. The results for various wall types, including drywall, brick, solid concrete, and cinder block, the latter two under both wet and dry conditions, are presented.

Received 10 September 2010, Accepted 4 May 2011, Scheduled 10 May 2011
Corresponding author: Christopher Thajudeen (christopher.thajudeen@villanova.edu).

1. INTRODUCTION

There exists much interest in the development of technologies, for both civilian and military applications, which are capable of imaging the interior of a building and subsequently identifying targets of interest, such as humans or weapon caches. Applications that can benefit from through-the-wall imaging and sensing include earthquake rescue, military surveillance, police and fire rescue operations, and hostile urban environment threat assessments. Of the many technologies that may prove useful in accomplishing the goals of through-the-wall systems, those employing electromagnetic (EM) waves, have been at the forefront of research in recent years [1–7]. The presence of walls adversely affects the ability of any conventional imaging technique to properly image targets enclosed within building structures. Recent work in the field of through-the-wall radar imaging (TWRI) aims to extend standard radar imaging techniques, such as imaging using synthetic aperture radar (SAR) [8, 9], to account for the presence of the wall, as well as enhance imaging performance through the incorporation of wideband sensor technologies [10].

Generally speaking, the ability of EM waves to penetrate a variety of building walls is at the core of TWRI systems. Although EM waves in the lower microwave bands can penetrate various common construction materials, such as brick, drywall, plywood, cinderblock, and solid concrete, the propagation through the wall can adversely affect the EM waves resulting primarily in attenuation and distortion due to dispersion [11–13]. Such wave distortions are further compounded when reinforcements, such as rebar, are present within the wall [14, 15] as well as when the wall material experiences high moisture level due to rain and or other environmental conditions. These distortions can cause errors in proper target radar cross section (RCS) registration during imaging. Effective approaches that achieve proper target RCS registration behind walls must exploit a detailed understanding of the radar phenomenology, in general, and more specifically, knowledge of the expected strength of the radar returns from targets of interest. In addition to understanding the wall phenomenology, imaging algorithms have been developed which can compensate for some wall effects through beamforming and auto-focusing of targets inside enclosed structures under known [3, 16–18] or unknown wall scenarios [19–23]. The emphasis of the present paper, therefore, is not on imaging techniques but rather on wall parameter measurement and its effect on TWRI required dynamic range power.

Fundamentally, knowledge of the range of possible power returns from targets behind walls must be considered so that the radar system

is designed with sufficient sensitivity to properly detect the targets of interest. Normally, to estimate a target's return power under various wall conditions, such as hydrated (wet) walls, rigorous testing must be performed for all targets of interest at different incident angle which is an expensive and time consuming endeavor. The objectives of this paper are therefore twofold: i) experimental characterization of the walls under various conditions, and ii) presentation of a simple method which employs a hybrid measurement and electromagnetic modeling approach for the estimation of power returns from targets of interest behind walls. Using the proposed method, it is possible to measure the walls under various conditions independent of a target and then determine its effects for any target of interest. This is a great savings in both time and cost during system development. The effects of various wall types and wall conditions, most notably hydration levels of solid concrete walls, on the received power of the target returns from several targets of interest including a human and an AK-47 rifle, are presented.

The paper is organized as follows. In Section 2, the constitutive parameters associated with various wall types are extracted using a free-space measurement technique. The reflection and transmission coefficients associated with each wall type are then determined for the measured constitutive parameters. Section 3 introduces a modified radar range equation, which analytically accounts for the wall effects, including multiple reflections within a given homogeneous or layered wall. The RCS associated with various targets, including a material-exact rifle and human model, are then calculated through the use of numerical electromagnetic modeling tools. The hybrid measurement and numerical approach is then used to estimate the received power versus frequency from the aforementioned targets for a concrete wall under various hydration levels. Section 4 contains the concluding remarks.

2. MEASURED WALL PARAMETERS

2.1. Measurement of Wall Constitutive Parameters

Table 1 lists the five wall materials chosen for this study. The materials were chosen as a representative set of the most commonly encountered building materials used in modern wall construction. The material thicknesses were chosen based on the standardized dimensions of readily available building supplies. In the case of plywood and drywall, the materials were assumed to be freestanding and no supports were taken into consideration. In the case of brick, solid concrete, and hollow concrete (cinder block), it was assumed that no mortar or reinforcements were used in the wall construction.

Table 1. Material dimensions.

Material	Description	Sample or Unit Dimensions of Material	Downrange Material Thickness	Condition Measured
Plywood	3 ply exterior	$1/2'' \times 24'' \times 24''$ $12.7 \times 610 \times 610$ mm	1/2 " 12.7 mm	Dry
Drywall		$1/2'' \times 24'' \times 24''$ $12.7 \times 610 \times 610$ mm	1/2 " 12.7 mm	Dry
Brick	Standard Modular Red Mattex	$35/8'' \times 21/4'' \times 75/8''$ $92 \times 57 \times 194$ mm	3 5/8" 92 mm	Non mortared joints, Dry
12" Hollow core concrete block	ASTM C33 C90 1900 PSI net	$113/4'' \times 73/4'' \times 153/4''$ $299 \times 197 \times 400$ mm	11 1/4 " 299 mm	Non mortared joints, Dry & Wet
6" solid concrete block	ATSM C33 C90 1900 PSI net	$53/4'' \times 73/4 \times 153/4''$ $146 \times 197 \times 400$ mm	5 1/4 " 146 mm	Non mortared joints, Dry & Wet

The constitutive parameters were measured using commercially available building products whose dimensions are specified in Table 1. The free-space technique for measuring the complex dielectric constant as a function of frequency was chosen as the measurement regime. The free-space method uses two broadband antennas, one on either side of a slab of wall material, and a network analyzer in S-parameter configuration for measurements. This method is non-contacting and readily lends itself to the testing of building materials.

Transmit and receive horn antennas were placed 1 m away on each side of the material under test (MUT), as illustrated in Figure 1. This distance was a compromise between far field conditions and illumination of the MUT by the antennas. In this setup, the Agilent Gated Reflect Line (GRL) Calibration [29] is used to first calibrate the test set-up and cables in the absence of the wall. The data was collected using an Agilent N5230A Network Analyzer and associated Agilent 85071E dielectric measurement software [29] over the frequency range from 1 to 3 GHz in 746 frequency steps. The Agilent software includes several algorithms to solve for the permittivity and permeability of the material under test. The key component of the free space measurement capability of the software is the ability to calibrate out unwanted responses from the test fixture designed to support the MUT as well as

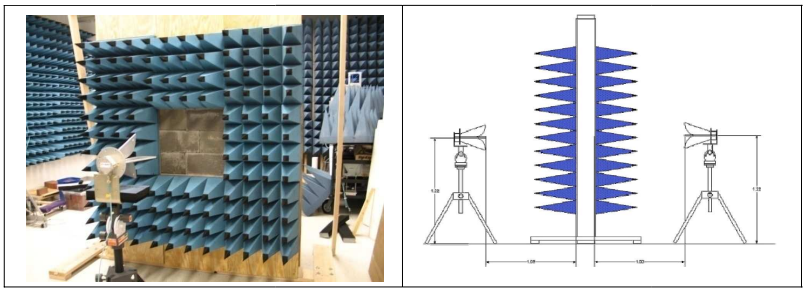

Figure 1. Setup for measurement of wall parameters.

the test antennas. For this work, the Transmission model was chosen. The Transmission model assumes the material to be measured is non-magnetic. In addition, as the measurement software indicates this model often converges to a solution when the other extraction models may fail, due primarily to the fact it only relies on the S_{11} measurement to derive a solution. The Transmission model can compute multiple solutions when the phase shift through the test sample is greater than -360°. This ambiguity can be resolved by providing the software with an estimate of the permittivity, ε_r', which can be derived by using the time domain response to get an average time delay $\Delta\tau$ through the material of thickness d as [30]

$$\varepsilon_r' \cong \left[1 + \frac{\Delta\tau}{d/c}\right]^2 \tag{1}$$

where c is the speed of light. Figure 2 depicts the measured permittivity, ε_r, and loss tangent, $\tan(\delta)$, for the five building materials of Table 1. For the inhomogeneous and composite materials, namely dry-wall and hollow concrete, Figure 2 represents the effective complex permittivity values for these walls assuming a homogeneous dielectric slab of the same thickness. The results in Figure 2 are in general agreement with those given in [31] for selected frequencies. Assuming the wall constitutive parameters are frequency independent, one can alternatively use the time-domain reflectometry technique in [32], which is particularly useful for parameters estimation of unknown walls in TWRI field operation.

The constitutive parameters were also measured for solid concrete and hollow concrete under various hydration (wetness) conditions. The wall was soaked completely so that the entire wall was evenly wet and the most water retention of the concrete was acquired. The constitutive parameters were then measured at different times during the drying period after no more water was being applied. The experimental measured data was collected at 0, 3, 6, 21, 25, 28, 30, and 47 hours.

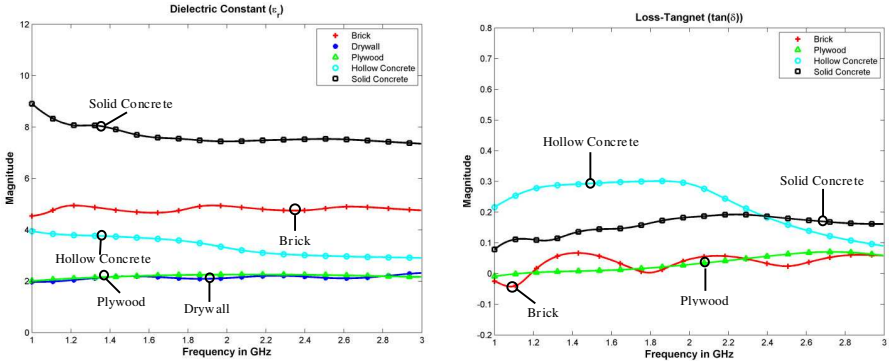

Figure 2. Measured (a) dielectric constant and (b) loss-tangent for plywood, drywall, brick, solid concrete, and hollow concrete.

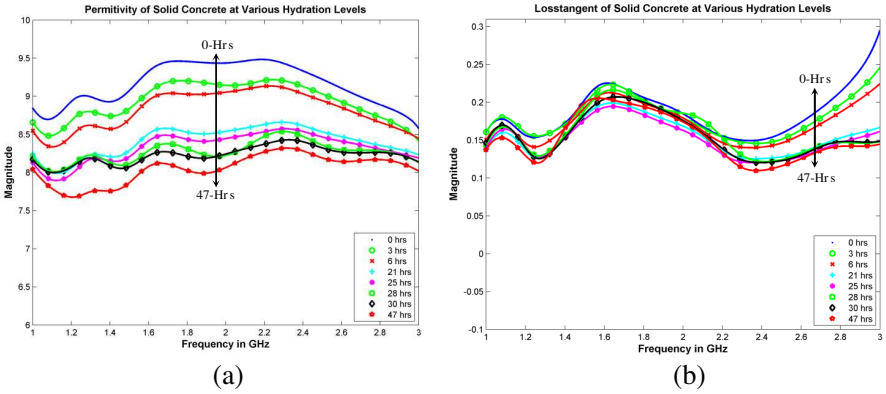

Figure 3. Measured (a) dielectric constant and (b) loss-tangent for solid concrete at 0, 3, 6, 21, 25, 28, 30, and 47 hours after initial hydration.

Figures 3 and 4 show the measured permittivity and loss tangent associated with the solid concrete wall and the hollow concrete wall at the various stages of hydration. As seen, under different wetness conditions, ε_r and $\tan(\delta)$ can vary significantly within the 1–3 GHz band. It is important to note that the dry solid concrete case in Figure 2 (measured before the wall was made wet) has a slightly different frequency profile when compared to the hydrated cases in Figure 3. This is due primarily to the fact that even at the 47 hrs mark, the concrete still retained enough moisture to be not considered completely "dry".

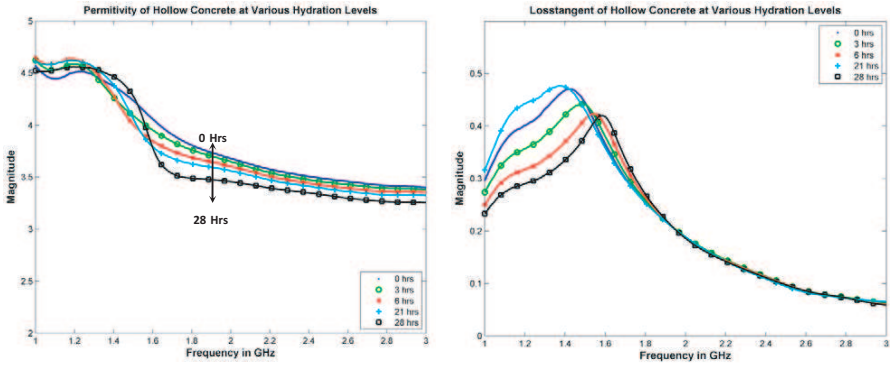

(a) (b)

Figure 4. Measured (a) dielectric constant and (b) loss-tangent for Hollow Concrete at 0, 3, 6, 21, and 28 hours after initial hydration.

3. POWER ESTIMATION USING A HYBRID EXPERIMENTAL-NUMERICAL TECHNIQUE

3.1. Modified Radar Range Equation

In order to properly estimate the power return from targets within building structures, the effects of the walls must be taken into account. Unlike a free space environment where the primary losses are due to the target materials and the roundtrip free-space path loss, the through-the-wall environment contains an obstacle in the form of a wall that introduces new losses due to the constitutive parameters of the wall materials. For most common wall materials, the parameters are frequency dependent resulting in dispersion and distortion of the transmitted signal as it passes through the wall. Additionally, the moisture content of the walls can affect the constitutive parameters and further distort the transmitted wave. It is necessary, therefore, to estimate the losses associated with the walls.

The typical bi-static radar composed of a pair of transmitting and receiving antennas, for use in imaging of a target in free-space, is shown in Figure 5(a). In this scenario, the losses in the system can be attributed to the free-space path losses, the target losses, and the polarization mismatch between the transmitting and receiving antennas. The ratio of the transmitted to received power can be expressed in terms of these losses as well as the gains associated with the receiving and transmitting antenna through the free-space radar range equation. The corresponding bi-static system used for through-the-wall target detection is shown in Figure 5(b). The addition

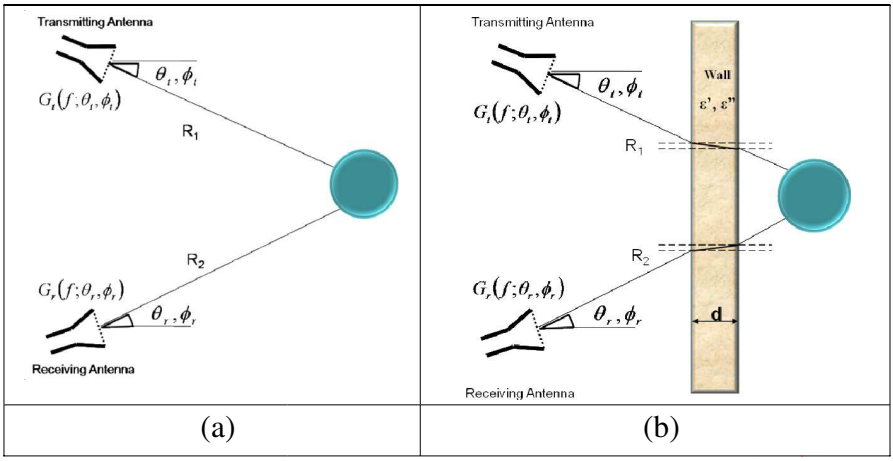

Figure 5. Typical bi-static radar (a) free-space and (b) through-the-wall scenario.

of the wall between the bi-static antenna system and the target of interest induces further losses, which are not encountered in the free-space scenario. In order to account for the additional losses due to the wall, the free-space radar range equation can be modified by adding the round-trip transmission losses through the wall. If it is assumed that the wall of Figure 5(b) is of infinite extent in the y-z plane, then the transmission losses can be accounted for by using the analytical expression for transmission coefficient T of the wall with given constitutive parameters ε_r, μ_r, and $\tan(\delta)$. For round-trip propagation, the wave encounters the wall twice; once from the transmit antenna to the target and then again from the target to the receive antenna. This process results in the original wave being modified twice by the transmission coefficient associated with the wall; once as a function of the transmit angles (θ_t, ϕ_t) and then as a function of the receive angles (θ_r, ϕ_r). Considering the general bi-static case where the transmit and receive angles are not equivalent, the modified Radar range equation can then be written as

$$\frac{P_t}{P_r} = \sigma(f;\theta_r,\phi_r;\theta_t,\phi_t)\,|T(f;\theta_t,\phi_t)|^2\,|T(f;\theta_r,\phi_r)|^2 \frac{G_t(f;\theta_t,\phi_t)G_r(f;\theta_r,\phi_r)}{4\pi}\left(\frac{\lambda}{4\pi R_r R_t}\right)^2 |a_w a_r|^2 \quad (2)$$

where λ is the free-space wavelength, σ is the target's free-space RCS, and G_t and G_r are the respective power gains associated with the transmitting and receiving antennas at distances R_t and R_r from the

target, respectively. The final term in (2) accounts for the polarization mismatch between the scattered wave and the receiving antenna, with complex unit-vectors a_w and a_r, respectively. It is worth noting that G_r and G_t are functions of frequency, f, as well as the respective azimuth $(\phi_r,\ \phi_t)$ and elevation $(\theta_r,\ \theta_t)$ angles with respect to the normal. The target's RCS, σ, is a function of frequency as well as the azimuth and elevation angles of both antennas as depicted in Figure 5. We note that the product of σ and the forward and backward wall transmission coefficients may be interpreted as the effective RCS of the target when positioned behind the wall. Although negligible for the cases presented in this paper, if it were needed the wave velocity correction due to the wall effect can be accounted for through proper calculation of R_t and R_r.

A simplification of (2) can be employed when the transmitting and receiving angles are equal, as is the case during monostatic operation. Under these conditions, the transmission coefficients in (2) are equal and thus can be replaced by the 4th power of the magnitude of the transmission coefficient. Furthermore, under monostatic operation the transmitting and receiving antennas are the same with no polarization mismatch, thus allowing the modified radar range equation to be further simplified. It should be noted that the modified radar range equation in (2) does not include the power reflected from the wall itself. The wall reflected power [33] is proportional to $|R|^2$, where R is the wall reflection coefficient given in (3a).

In order to properly employ (2) the expressions for the reflection and transmission coefficients of a lossy dielectric slab can be used. Although the transmission and reflection coefficients can be easily determined for a multi-layer wall scenario, as depicted in Figure 6, this is not necessary for this study since the walls considered here are either physically composed of a single layer or effectively may be considered a single layer since the corresponding measured complex permittivity used in our formulation assumes a single dielectric slab model in the free-space parameter extraction outlined in Section 2. In general, it is well-known that the reflection and transmission coefficients, Γ and T, of an N-layer wall can be developed iteratively by considering the geometry of Figure 6 wherein a uniform plane wave is incident at an oblique angle θ_o with respect to the normal to the front of the wall.

For the general case of a N layer multi-layer wall depicted in Figure 6, the reflection and transmission coefficients can be written as:

$$\Gamma = \left[\frac{Y_0 - (C/B)}{Y_0 + (C/B)}\right] \tag{3a}$$

$$T = \left(\frac{2Y_0}{Y_0 B + C}\right) \tag{3b}$$

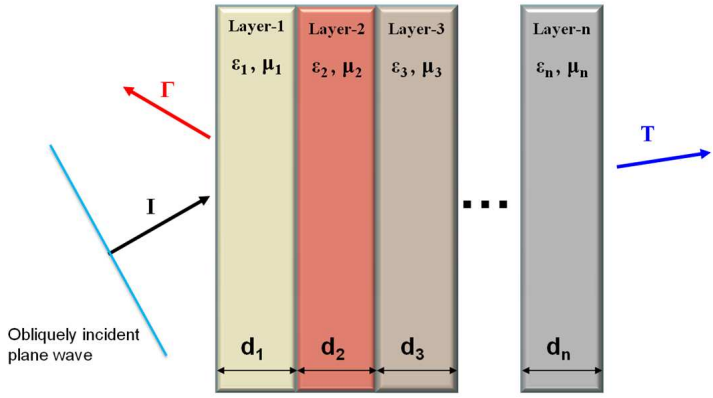

Figure 6. Multi-layer wall configuration.

where the values of C and B can be found from

$$\begin{bmatrix} B \\ C \end{bmatrix} = \left(\begin{bmatrix} A_1 & B_1 \\ C_1 & D_1 \end{bmatrix} \begin{bmatrix} A_2 & B_2 \\ C_2 & D_2 \end{bmatrix} \begin{bmatrix} A_3 & B_3 \\ C_3 & D_3 \end{bmatrix} \cdots \begin{bmatrix} A_N & B_N \\ C_N & D_N \end{bmatrix} \right) \begin{bmatrix} 1 \\ Y_o \end{bmatrix} \quad (4)$$

And the ABCD matrix associated with the nth layer can be expressed as:

$$\begin{bmatrix} \mathrm{A_n} & \mathrm{B_n} \\ \mathrm{C_n} & \mathrm{D_n} \end{bmatrix} = \begin{bmatrix} \cosh(\gamma_n d_n) & \frac{\sinh(\gamma_n d_n)}{Y_n} \\ Y_n \sinh(\gamma_n d_n) & \cosh(\gamma_n d_n) \end{bmatrix} \quad (5)$$

with

$$\gamma_n(f) = \frac{j\omega}{c} \sqrt{\tilde{\varepsilon}_{\mathrm{r}} n(f) - \sin^2(\theta_0)} \quad (6)$$

$$Y_1 = \begin{cases} \dfrac{\sqrt{\tilde{\varepsilon}_{r1}(f) - \sin^2\theta_o}}{\eta_o \tilde{\varepsilon}_{r1}(f)} & , \text{ for TE case} \\ \dfrac{1}{\eta_o \sqrt{\tilde{\varepsilon}_{r1}(f) - \sin^2\theta_o}} & , \text{ for TM case} \end{cases} \quad (7)$$

$$Y_0 = \frac{1}{\eta_0 \cos(\theta_0)} \quad , \qquad \text{for TE or TM case} \quad (8)$$

The complex relative permittivity in (6)–(7) can be expressed in terms of its relative permittivity ε_r and loss tangent $\tan(\delta)$ as

$$\tilde{\varepsilon}_r = \varepsilon_r(1 - j\tan(\delta)). \quad (9)$$

It should be noted that, in the case of cinder blocks, the wall is no longer homogeneous as it now contains multiple air-dielectric interfaces and, thus, must be considered as heterogeneous. The introduction of the internal air-dielectric boundaries produces multiple reverberations and Bragg effects, which, strictly speaking, require that the cinder

block be taken as an anisotropic medium. In order to represent this anisotropic medium in the power estimations preformed herein, measured material parameters are considered, which represent the effective values of the constitutive parameters, for a given polarization, when the cinder block is assumed to be a single layer lossy homogeneous slab. Under this assumption, the effective parameters then can be used with Equations (3a) and (3b) to generate the associated reflection and transmission coefficients for a cinder block wall.

3.2. Numerical RCS Simulations of Human and AK-47

The received power estimation from a target behind the wall in (2) requires the knowledge of the RCS of the target in freespace. In general, the RCS of a target is defined under plane wave illumination conditions. In practice, the plane wave illumination criterion can be approximated only when the target is placed a sufficient distance away from the source so that it can be considered as residing in the far-field of the same source. For canonical objects, such as a conducting sphere or a rectangular plate, the RCS can be either exactly or approximately modeled using available analytical expressions available in the literature [24–26]. For many targets of interest in through-the-wall radar imaging, however, the target RCS has to be numerically evaluated. For TWRI scenarios, targets such as humans and weapons are of great interest as their detection is paramount for both civilian and military applications. The RCS associated with these two complex targets are investigated through the use of numerical electromagnetic modeling tools. These targets, together with a sphere and rectangular plate, represent a diverse collection, which is very useful for practical through-the-wall radar power estimation scenarios.

We have employed full-wave electromagnetic modeling to numerically evaluate the many interactions and material effects which are not present in simple metallic structures. In the case of a human target, for example, the plethora of dielectric values and the inherent asymmetric distribution of materials within the body result in a highly complex system with an associated radar cross section that must be simulated numerically. In the case of a rifle, even though the total number of dielectric materials used in its construction is on the order of two or three, the complex features and geometry make it a prime candidate for numerical RCS evaluation.

The rifle model chosen for evaluation was that of an Avtomat Kalashnikova model 47 (AK-47) selective fire assault rifle. The AK-47 was chosen due to its pervasiveness throughout many regions where TWRI systems may be deployed. The model consisted of two materials, namely metal and wood. The metallic components

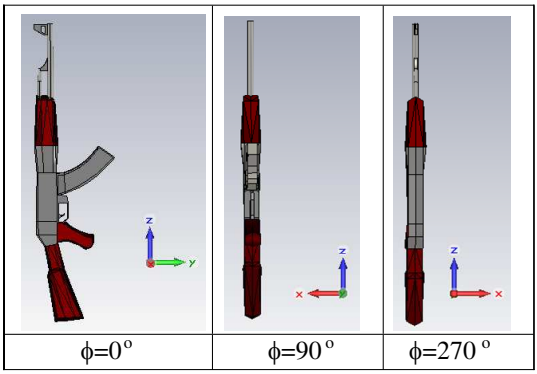

Figure 7. CAD model of an AK-47 selective fire rifle.

were treated as perfect electric conductors (PEC) while the wooden components were assigned a permittivity ($\varepsilon_r = 2$) and were chosen to be lossless. The AK-47 model had associated dimensions of height, width, and thickness equal to 894 mm, 256 mm, and 60 mm, respectively. For this study, the AK-47 model was simulated for three primary orientation angles in order to determine which of these would yield the largest RCS for demonstration purposes. Figure 7 depicts the CAD model of the AK-47, for the three primary orientation angles. The spherical coordinates were taken such that the θ angle was measured from the positive z-axis toward the x-y plane and the ϕ angle was measured from the positive x axis toward the y-z plane. The AK-47 model was numerically modeled using REMCOM's XFDTD simulation tool, which employs a Finite Difference Time Domain (FDTD) algorithm to solve complex geometries [27, 28]. For simulation purposes a frequency band wider than 1–3 GHz was investigated in order to determine the frequency trend of the AK-47 RCS. Along these lines, the frequency band of interest was chosen to be from 1 GHz to 6 GHz. In order to avoid numerical dispersion, at the upper band of interest, the XFDTD cell size was chosen to be 3 mm. This cell size resulted in a maximum calculation frequency of 10 GHz. The solution space for the AK-47 model was padded with 20 cells (60 mm) on each side to allow for proper calculations.

In addition to the AK-47, a high-fidelity CAD model of a human was also investigated using XFDTD for four primary orientations, namely, 0°, 90°, 180°, and 270°. The HiFi male human model is made up of 2.9 mm cubical FDTD mesh cells and 23 different tissue types. This model was chosen for its accurate representation of body materials, placement of organs, and bone locations. The model

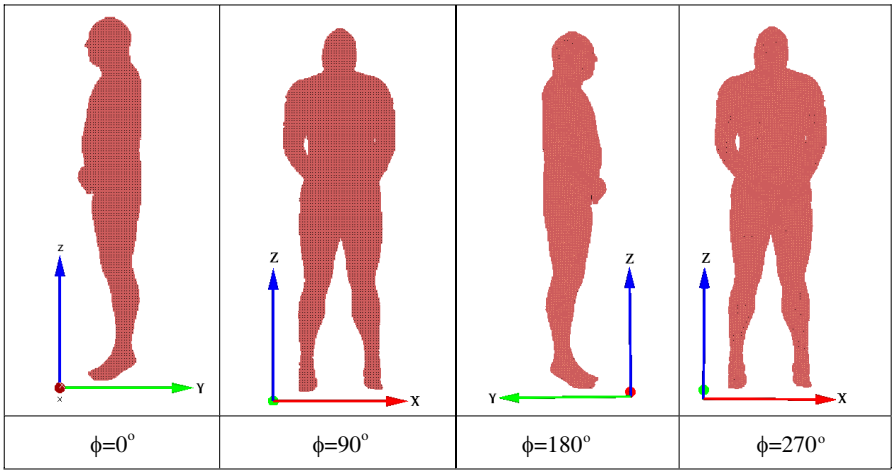

Figure 8. CAD model of HiFi human.

geometry had height, width, and depth dimensions of 1.88 m × 0.57 m × 0.324 m. The human model was padded with 20 cells (60 mm) on all sides. Figure 8 shows the HiFi human model at the four primary orientation angles.

The same incident waveform was used for both the AK-47 and HiFi Human RCS investigation. The time step (Δt) of the incident signal was chosen to be 5.757 ns with a total pulse width of $50 * \Delta t$. For consistency, both targets were assumed to be in the far field of the radiating source allowing the simulation excitation to be that of a plane wave with amplitude 1 V/m and an associated electric field polarity in the E_θ direction along the $+z$ axis. The incident waveform was chosen to be a modulated Gaussian with frequency content above 10 dB over the range of 0.5 GHz to 10.0 GHz.

The RCS was collected for the three primary orientation angles of 0°, 90° and 270° around the AK-47 with the addition of the 180° orientation angle for the human. For each orientation, the incident angle and the collected angle were the same (i.e., monostatic operation). Figure 9 shows the radar cross section versus frequency for the AK-47 and HiFi Human models. In lieu of measured RCS values for a real AK-47, an analogue model was constructed using a plastic AK-47 with metallic paint on the portions of the model corresponding to the metallic parts of the actual rifle. The measured RCS of this constructed model is included for comparison in Figure 9(a) for the 0° angle case. As seen, there is a relatively good agreement between the measured and FDTD simulated data up to about 5 GHz. As expected,

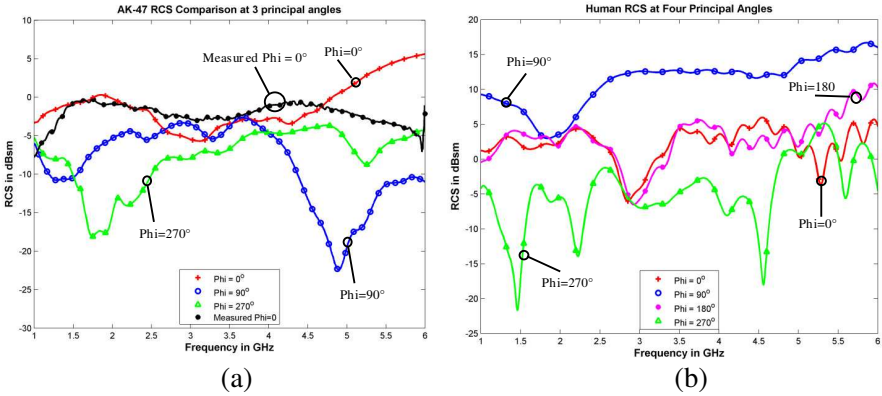

Figure 9. (a) AK-47 RCS vs. frequency at 0°, 90°, and 270° degrees; (b) human RCS vs. frequency at 0°, 90°, 180°, and 270°.

however, this crudely constructed model, which does not include all the detailed features of the real AK-47 (included in the FDTD model), fails in estimation of RCS values at higher frequency ranges.

3.3. Results Using Hybrid Approach

To properly estimate the power return from a target behind a wall, the modified Radar range equation of (2) can be employed. In order to do so effectively, knowledge of the wall transmission coefficient (T), the target's free-space radar cross section (σ), and the antennas' gain ($G_{r,t}$) and polarization ($a_{r,w}$) must be known. The wall transmission coefficient can be determined from (3b) utilizing the constitutive parameters which were measured for various wall types in Section 2. For homogeneous walls, the constitutive parameters, measured using the free-space method, are ideally independent of wall thickness and the incident angle. It is, therefore, possible to use (3b) for any arbitrary wall thickness and incident angle once the measured complex permittivity, $\tilde{\varepsilon}_r$, of the wall is known. As was discussed in Section 3.2, the free-space RCS can be found through the use of analytical or numerical models. The ability to generate free-space radar cross sections using numerical electromagnetic simulation tools is desirable because it allows for the calculation of very complex targets without having to physically acquire the targets in question. Using both the measured wall characteristics and modeled free-space target RCS, it is possible to utilize (2) to model the power return from any of the aforementioned targets of interest behind various walls used in practice.

The key component of (2), which characterizes the effect of the

wall on a specific target RCS under monostatic operation, is the factor $\sigma|T|^4$. Due to the fact that this factor only consists of the wall transmission coefficient and the target RCS, it can serve as a useful metric for determining the effect of the wall on the target RCS. For the purpose of verification a numerical simulation was performed, using ANSOFT Designer, which consisted of a rectangular PEC plate behind a solid concrete wall. The PEC plate had a length and width of 40 cm × 40 cm and was placed at various distances behind a solid concrete wall. The simulated wall had a downrange thickness of 146 mm, and a frequency independent permittivity of $\varepsilon_r = 7.66$ which corresponds to the average permittivity of the measured solid concrete wall as presented in Figure 2. The simulation was performed for both a lossless case ($\tan(\delta) = 0$) and a lossy frequency independent case ($\tan(\delta) = 0.157$) where the value of the loss tangent was taken to be the average of the measured loss tangent for the solid concrete wall depicted in Figure 2. For both the lossless and lossy case, the target was placed at 10λ behind the wall when λ was calculated at 1 GHz. Since the proposed method assumes the target is in the far-field, further simulations were performed in order to investigate the effect of placing the target at distances such that it was no longer in the far-field. The target was simulated at distances of $\lambda/3$, 1λ, and 3.3λ behind both the lossless and lossy concrete walls. The resulting target RCS, modified by the wall, corresponds to the $\sigma|T|^4$ metric mentioned previously. As such, for comparison purposes, the $\sigma|T|^4$ factor was calculated analytically for a rectangular PEC plate placed behind both a lossless and lossy wall with the same dimensions as the aforementioned numerical simulation. Figure 10 compares the analytical and numerically simulated $\sigma|T|^4$ values over a 1 GHz to 3 GHz frequency range.

It is clear from Figure 10 that the analytical and 10λ case have a good agreement in $\sigma|T|^4$ in both the lossless and lossy wall cases. As the target is moved closer to the wall it is apparent that the analytical model is within an acceptable margin of error for the 3.3λ case, however it is not sufficient to account for the near-field effects clearly depicted by both the 1λ and $\lambda/3$ cases. The proposed hybrid (aggregate) approach, therefore, should be used primarily for targets in the far-field and will acceptably approximate targets at distances slightly short of far-field. It should not, however, be considered accurate enough to be used for targets within the near-field. With this constraint in mind, all following examples are for targets in the far-field. Figure 11 depicts the $\sigma|T|^4$ metric for various wall types and the four targets of interest. The orientation angles of the AK-47 and Human models used for Figure 11, and all subsequent figures, correspond to 0° and 90° respectively.

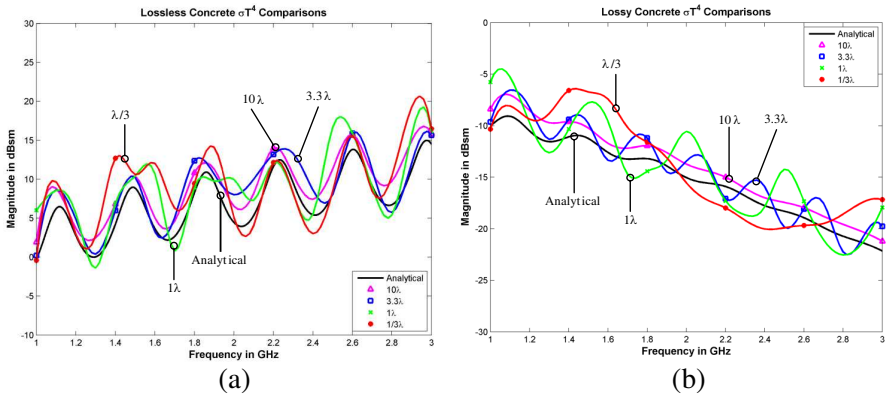

Figure 10. Comparison of analytical and numerically simulated $\sigma|T|^4$ at different target distances vs. frequency for a rectangular PEC plate behind a (a) lossless and (b) lossy solid concrete wall.

In order to assess the power returns, helpful in system design considerations, in a typical TWRI scenario, the received power from all four targets (sphere, rectangular plate, AK-47, and Human), when placed behind the five wall types, are calculated using the proposed hybrid approach. The power estimation calculations are performed assuming the monostatic radar operation. For all results presented hereafter, the distance between the transmit/receive antenna and the target is taken to be 5 m, which represents common standoff distance for TWRI, and the antenna is assumed to be a standard gain horn antenna with a gain of 10 dBi. Figure 12 depicts the received power from the four targets over the frequency band of interest, from 1 GHz to 3 GHz, for brick, drywall, cinder block, solid concrete, and plywood, denoted by $(+, \bullet, \mathrm{o}, \blacktriangle, *)$ respectively. These results clearly show that a system dynamic range of better than -80 dB is desired for detection of the human and AK-47 targets behind solid and hollow concrete walls in the 1–3 GHz frequency band. We note that Figures 11 and 12 are depicting the effective RCS of the targets in the presence of the walls and the received power for a given wall-target combination respectively. As such, these plots do not give any information about locating or identifying the targets. They should be used as a guide to system development to determine the power return levels for wall-target combinations of interest.

The results in Figure 12 correspond to a monostatic situation where it is assumed that all target's aspect angles are within the antenna's main beam and within a few degrees from the normal angle of $\theta = 0°$. For a bistatic TWRI scenario both wall transmission

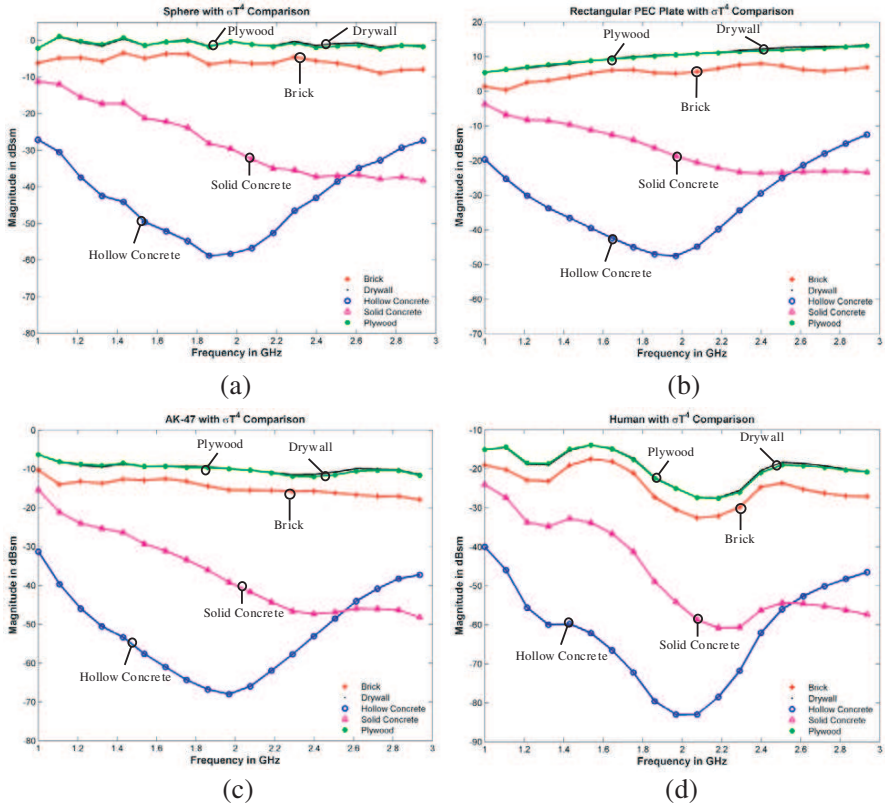

Figure 11. $\sigma|T|^4$ vs. frequency for (a) sphere, (b) rectangular plate, (c) AK-47, (d) human.

coefficients, T_t and T_r, and the target's RCS dependence on transmit and received angles in (2) affect the received power. To show the decrease in power levels for off-normal incident and received angles we have plotted the received power for the example of a square PEC plate in Figure 13, now assuming that the transmit and the receive antennas are located at $\theta_t = \theta$ and $\theta = -\theta$ with respect to the normal incidence. The results are plotted for $\phi_t = \phi_r = 0°$. As seen, the received power in this case drops as much as 10 dB, for the plywood wall, and 18 dB, for the concrete wall, as θ varies from 0 to 75 degrees. We note that due to the symmetry of the target geometry and the symmetric positioning of transmit and receive antennas in this example, the reduction in power is mainly due to the wall transmission coefficient and not the angular dependence of the target's RCS.

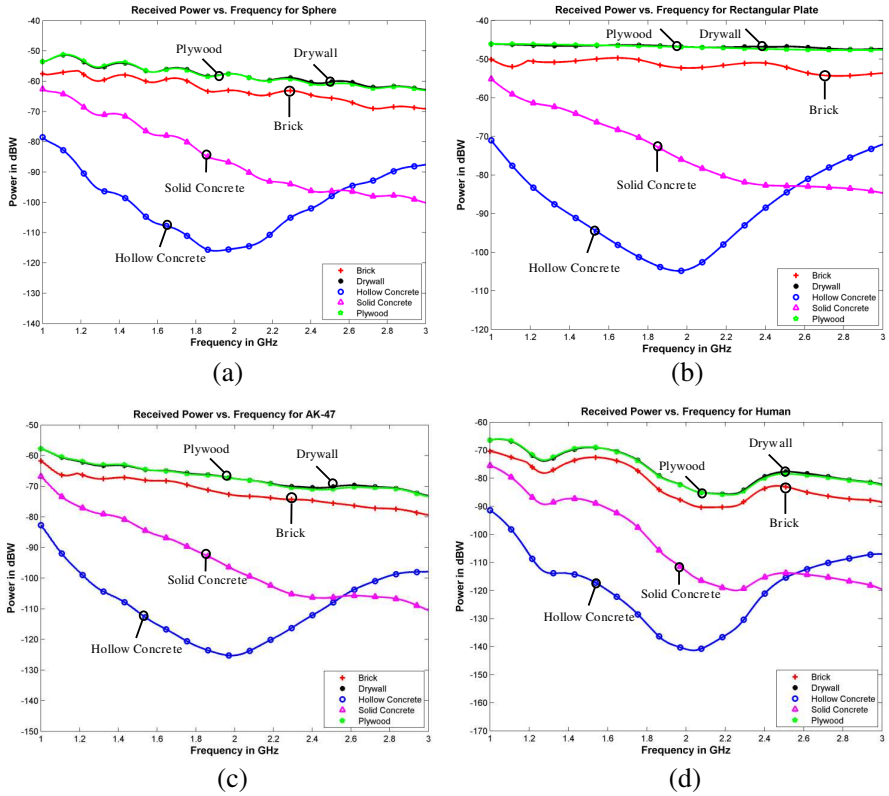

Figure 12. Wall effects on received power for (a) sphere, (b) rectangular plate, (c) AK-47, (d) human.

It is desirable to understand the effects of the hydration (wetness) of building walls on the received power from targets of interests behind walls for various through-the-wall imaging applications. As previously stated, with the above aggregate approach it is not necessary that each target be measured behind the wall during each stage of hydration. Rather, it is only necessary that the constitutive parameters be measured at each stage. The wall transmission coefficient can then be determined for the new parameters and applied to the modified radar range equation of (2). This greatly reduces the time required to calculate power returns as compared to the conventional method wherein it is necessary to measure or numerically compute each target behind every wall type under different wall conditions independently.

To demonstrate the effects of hydration on typical TWRI power returns, a solid concrete wall was chosen. The measured constitutive

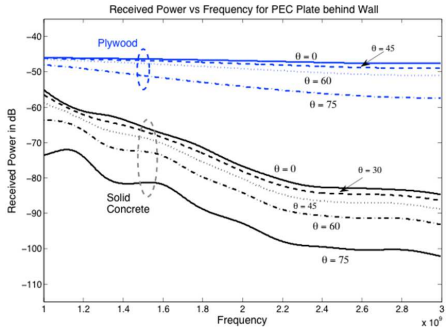

Figure 13. Wall effects on bi-static received powers for rectangular plate target behind plywood and concrete walls.

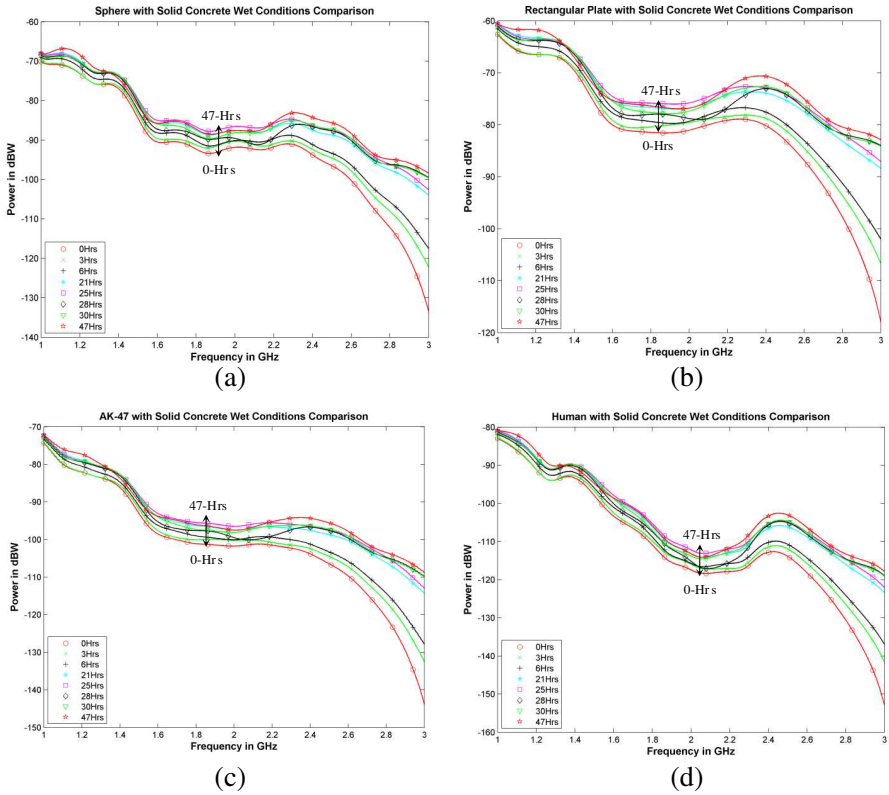

Figure 14. Targets behind solid concrete with various wet conditions with (a) sphere, (b) rectangular plate, (c) AK-47, (d) human.

parameters were used in the power calculations. Figure 14 depicts the estimated power returns from the four targets in question over the 1 GHz to 3 GHz frequency band at various stages during the drying period. As previously stated, the orientation angles of the AK-47 and Human models correspond to 0° and 90° respectively. It is apparent from Figure 14 that as the moisture content decreases from the 0-hour case to the 47-hour case, the received power decreases by about 3 dB at 1 GHz and as much as 30 dB at 3 GHz for all four targets of interest.

4. CONCLUSION

In this paper, measured results for complex permittivity of some commonly used walls under different hydration (wetness) conditions were presented and a new simple approach for the estimation of power returns from targets of interest located behind building walls was discussed. In particular, a frequency-domain wall parameter measurement system was employed to measure constitutive parameters for drywall, plywood, brick, cinder block, and concrete block walls under different hydration conditions, which can then be used to determine the transmission and reflection coefficients analytically for a wall of arbitrary thickness and for different incident angles. The measured wall parameters and modeled free-space target radar cross sections, notably those of a material accurate AK-47 assault rifle and a high-fidelity human model, were subsequently used in combination with a modified radar range equation to determine the return power from various targets of interest when they were placed behind the aforementioned wall types. This simple hybrid approach to target power estimation for TWRI applications was also employed in the study of the effect of moisture content in solid concrete blocks on the returned power levels for the considered targets. It was found that high moisture content in solid concrete walls can decrease the received power of a target of interest by as much as 18 to 20 dB within the 1–3 GHz band. The proposed hybrid model offers a robust method for determining the power returns from a target of interest in a through-the-wall imaging environment. In particular, the ability to use measured wall constitutive parameters in conjunction with the known or modeled free-space RCS of a target can readily yield insights into the effects of various physical wall conditions on the power return from any complex target, which may be helpful in design of TWRI systems with scenario-specific dynamic range.

ACKNOWLEDGMENT

The authors would like to thank Mr. Paul Rush (NAVSEA) and Mr. Bill Ailes (Wyle Labs) for their help in performing the permittivity measurements of various walls. This work was supported in part by DARPA under contract HR0011-06-C-0110, and in part by Army Research Lab under contract W911NF-07-D-0001. Approved for public release. Distribution unlimited.

REFERENCES

1. Borek, S. E., "An overview of through the wall surveillance for homeland security," *Proc. 34th Appl. Imagery Pattern Recognition Workshop*, Washington, DC, 2005.
2. Amin, M., "Special issue on 'Advances in indoor radar imaging'," *J. Franklin Inst.*, Vol. 345, No. 6, 556–722, 2008.
3. Baranoski, E. and F. Ahmad, "Special session on 'Through-the-wall radar imaging'," *Proc. 2008 IEEE Int. Conf. Acoust., Speech, Signal Process.*, Las Vegas, NV, 2008.
4. Baranoski, E., "Through-wall imaging: Historical perspective and future directions," *J. Franklin Inst.*, Vol. 345, No. 6, 556–569, 2008.
5. Farwell, M., J. Ross, R. Luttrell, D. Cohen, W. Chin, and T. Dogaru, "Sense through the wall system development and design considerations," *J. Franklin Inst.*, Vol. 345, No. 6, 570–591, 2008.
6. Ferris, Jr., D. and N. Currie, "A survey of current technologies for through-the-wall surveillance (TWS)," *Proc. SPIE*, Vol. 3577, 62–72, 1998.
7. Black, J., "Motion and ranging sensor through-the-wall surveillance system," *Proc. SPIE*, Vol. 4708, 114–121, 2002.
8. Ahmad, F., M. Amin, and S. Kassam, "Synthetic aperture beamformer for imaging through a dielectric wall," *IEEE Trans. Aerosp. Electron. Syst.*, Vol. 41, No. 1, 271–283, 2005.
9. Ahmad, F., S. Kassam, and M. Amin, "Practical considerations for the design of a wideband synthetic aperture beamformer," *Proc. IEEE International Symposium on Antennas and Propagation*, Vol. 3B, 318–321, 2005.
10. Withington, P., H. Fluhler, and S. Nag, "Enhancing homeland security with advanced UWB sensors," *IEEE Microw. Mag.*, Vol. 4, No. 3, 51–58, Sep. 2003.
11. Holloway, C., P. Perini, R. DeLyser, and K. Allen, "Analysis

of composite walls and their effects on short-path propagation modeling," *IEEE Trans. on Vehicular Tech.*, Vol. 46, No. 3, 730–738, 1997.

12. Zwick, T., J. Haala, and W. Wiesbeck, "A genetic algorithm for the evaluation of material parameters of compound multilayered structures," *IEEE Transactions on Microwave Theory and Techniques*, Vol. 50, No. 4, 1180–1187, 2002.
13. Honcharenko, W. and H. Bertoni, "Transmission and reflection characteristics at concrete block walls in the UHF bands proposed for future PCS," *IEEE Transactions on Antennas and Propagation*, Vol. 42, No. 2, 232–239, 1994.
14. Dalke, R., C. Holloway, P. McKenna, M. Johansson, and A. Ali, "Effects of reinforced concrete structures on RF communications," *IEEE Transactions on Electromagnetic Compatibility*, Vol. 42, No. 4, 486–496, 2000.
15. Richalot, E., M. Bonilla, M.-F. Wong, V. Fouad-Hanna, H. Baudrand, and J. Wiart, "Electromagnetic propagation into reinforced-concrete walls," *IEEE Transactions on Microwave Theory and Techniques*, Vol. 48, No. 3, 357–366, 2000.
16. Dehmollaian, M. and K. Sarabandi, "Refocusing through building walls using synthetic aperture radar," *IEEE Trans. Geosci. Remote Sens.*, Vol. 46, No. 6, 1589–1599, 2008.
17. Soldovieri, F. and R. Solimene, "Through-wall imaging via a linear inverse scattering algorithm," *IEEE Geoscience and Remote Sensing Letters*, Vol. 4, No. 4, 513–517, Oct. 2007.
18. Zhang, W., C. Thajudeen, and A. Hoorfar, "Polarimetric through-the-wall imaging," *2010 URSI International Symposium on Electromagnetic Theory (EMTS)*, 471–474, Aug. 16–19, 2010.
19. Wang, G. and M. Amin, "Imaging through unknown walls using different standoff distances," *IEEE Trans. on Signal Processing*, Vol. 54, No. 10, 4015–4025, 2006.
20. Ahmad, F., M. Amin, and G. Mandapati, "Autofocusing of through-the-wall radar imagery under unknown wall characteristics," *IEEE Transactions on Image Processing*, Vol. 16, No. 7, 1785–1795, 2007.
21. Ahmad, F. and M. Amin, "Analyses of autofocusing schemes for indoor imaging with unknown walls," *Fourth IEEE Workshop on Sensor Array and Multichannel Processing*, 358–362, 2006.
22. Dehmollaian, M. and K. Sarabandi, "Analytical, numerical, and experimental methods for through-the-wall radar imaging," *IEEE Int. Conf. Acoust., Speech, Signal Process.*, 5181–5184, 2008.

23. Wang, G., M. Amin, and Y. Zhang, "New approach for target locations in the presence of wall ambiguities," *IEEE Transactions on Aerospace and Electronic Systems*, Vol. 42, No. 1, 301–315, 2006.
24. Skolnick, M., *Introduction to Radar Systems*, McGraw-Hill, 1980.
25. Knott, E., M. Tuley, and J. Shaeffer, *Radar Cross Section*, 2nd edition, SciTech Publishing, 2004.
26. Balanis, C., *Advanced Engineering Electromagnetics*, Jon Wiley & Sons, Inc., New York, 1989.
27. [Online]. Available: http://www.remcom.com/xfdtd/optional-modules/biological-meshes.html.
28. [Online]. Available: http://www.remcom.com/xf7.
29. Agilent 85071E Material Measurement Software, http://cp.literature.agilent.com/litweb/pdf/5988-9472EN.pdf.
30. Amin, M., *Through-the-wall Radar Imaging*, 1–32, CRC Press, 2010.
31. Safaai-Jazi A., S. M. Riad, A. Muqaibe, and A. Bayram, "Ultra-wideband propagation measurements and channel modeling," Technical Report, Bradley Department of Electrical Engineering, Virginia Polytechnic Institute and State University, Nov. 2002.
32. Aftanas, M., J. Sachs, M. Drutarovsky, and D. Kocur, "Efficient and fast method of wall parameter estimation by using UWB radar system," *Frequenz Journal*, 231–235, Vol. 63, No. 11–12, Germany, Nov. 2009.
33. Landron, O., M. Feuerstein, and T. Rappaport, "In situ microwave reflection coefficient measurements for smooth and rough exterior wall surfaces," *IEEE 43rd Vehicular Technology Conference*, 77–80, 1993.